CANCER

Noninvasive ovarian cancer biomarker detection via an optical nanosensor implant

Ryan M. Williams,[1] Christopher Lee,[1] Thomas V. Galassi,[1,2] Jackson D. Harvey,[1,2] Rachel Leicher,[3,4] Maria Sirenko,[1] Madeline A. Dorso,[1,2] Janki Shah,[1] Narciso Olvera,[5] Fanny Dao,[5] Douglas A. Levine,[5] Daniel A. Heller[1,2]*

Patients with high-grade serous ovarian carcinoma (HGSC) exhibit poor 5-year survival rates, which may be significantly improved by early-stage detection. The U.S. Food and Drug Administration–approved biomarkers for HGSC—CA-125 (cancer antigen 125) and HE4 (human epididymis protein 4)—do not generally appear at detectable levels in the serum until advanced stages of the disease. An implantable device placed proximal to disease sites, such as in or near the fallopian tube, ovary, uterine cavity, or peritoneal cavity, may constitute a feasible strategy to improve detection of HGSC. We engineered a prototype optical sensor composed of an antibody-functionalized carbon nanotube complex, which responds quantitatively to HE4 via modulation of the nanotube optical bandgap. The complexes measured HE4 with nanomolar sensitivity to differentiate disease from benign patient biofluids. The sensors were implanted into four models of ovarian cancer, within a semipermeable membrane, enabling the optical detection of HE4 within the live animals. We present the first in vivo optical nanosensor capable of noninvasive cancer biomarker detection in orthotopic models of disease.

INTRODUCTION

Worldwide, more than 238,000 patients are diagnosed with ovarian cancer, a disease that is responsible for more than 151,000 deaths each year (*1*, *2*). Ovarian cancer is the fifth leading cause of cancer-related deaths among females in the United States and first among gynecologic malignancies (*3*). These grim statistics are due in part to the advanced stage at which most cases are detected—at stage III or later in more than 60% of diagnoses—higher than any other form of cancer (*3*–*5*). Among all populations, the 5-year survival rate is just 46% (*5*). In cases where diagnosis occurs at stage I, however, the 5-year survival rate is 92% (*6*). Current screening methods involve cancer antigen 125 [CA-125 or mucin 16 (MUC16)] serum testing and transvaginal ultrasonography. However, the U.S. Preventive Services Task Force recommends against these methods because of high false-positive rates and poor sensitivity for detecting small lesions (*7*). These methods neither alter patient outcome nor reduce mortality (*8*). Consequently, new methods are needed to detect early-stage disease to reduce the burden of ovarian cancer (*9*).

Human epididymis protein 4 (HE4) is one of two U.S. Food and Drug Administration–approved serum biomarkers for ovarian cancer, along with CA-125, and is involved in ovarian tumorigenesis (*10*). This protein is overexpressed by malignant epithelial cells (*11*) and is found in increased levels in patient serum (*12*, *13*), ascites (*14*), and uterine fluid (*15*, *16*). Serum-based HE4 provides similar sensitivity and specificity for ovarian cancer diagnosis as CA-125, although it may be more useful in differentiating benign from malignant disease (*12*). Like CA-125, data do not show that serum-based screening for HE4 improves overall patient survival. However, uterine cavity concentrations of these markers are greater (23-fold greater median values for HE4) than serum concentrations and may therefore present a route for more sensitive ovarian cancer detection than serum-based measurements (*15*, *16*).

Implantable sensors are of increasing interest for the detection of disease biomarkers. Distinct from imaging agents used to visualize disease sites or delineate disease versus normal tissue for surgery (*17*), implantable sensors aim to quantify biomarkers via devices that normally remain stationary in the body. Progress in electronic implants includes the development of increasingly flexible and thin electronic materials (*18*). Optical implantable sensors include quantum dot-based ion-selective sensors (*19*) and pH sensors (*20*).

Single-walled carbon nanotubes (SWCNTs) have electronic and optical properties that are well suited for in vivo signal transduction. Semiconducting carbon nanotubes emit near-infrared (NIR) bandgap photoluminescence (PL) between 800 and 1600 nm (*21*), which can penetrate living tissues to a distance in the centimeter range (*22*). Carbon nanotubes have been investigated for use in vivo to image vasculature and as intraoperative probes (*17*). Carbon nanotube fluorescence exhibits unique photostability (*23*), allowing for repeated, long-term measurements. Nanotubes also exhibit exquisite sensitivity to their local environment via optical bandgap modulation (*24*). Previous works have demonstrated the optical detection of small molecules (*25*) and proteins (*26*) in or on live cells (*24*). Nanotubes have been used in vivo to detect nitric oxide in the liver of live murine models of inflammation (*27*) and exogenous microRNA (*28*).

Here, we developed a carbon nanotube–based sensor to optically detect the ovarian cancer biomarker HE4 in vivo. The sensor was developed by derivatizing NIR-emitting carbon nanotubes to transduce the binding of HE4 to an immobilized antibody. The antibody-nanotube complex responded specifically to HE4 via modulation of the nanotube emission wavelength. Responses from single nanotubes differentiated high-grade serous ovarian carcinoma (HGSC) from control patient serum and ascites samples. We then engineered an implantable device incorporating the antibody-nanotube complex and surgically implanted it into mice. The implant could be probed noninvasively via NIR optical excitation and collection. The device successfully quantified exogenously derived HE4 and detected endogenous HE4 in orthotopic

[1]Memorial Sloan Kettering Cancer Center, New York, NY 10065, USA. [2]Weill Cornell Medicine, Cornell University, New York, NY 10065, USA. [3]Tri-Institutional Program in Chemical Biology, New York, NY 10065, USA. [4]The Rockefeller University, 1230 York Avenue, New York, NY 10065, USA. [5]Laura and Isaac Perlmutter Cancer Center, NYU Langone Medical Center, New York, NY 10016, USA.
*Corresponding author. Email: hellerd@mskcc.org

murine models of ovarian cancer to differentiate HE4-producing models from HE4-deficient models (*11*).

RESULTS

We developed a carbon nanotube–based sensor for HE4 by synthesizing a stable anti-HE4 antibody-nanotube complex without chemical perturbation of the graphitic carbon of the nanotube (Fig. 1A). SWCNTs [Unidym high pressure carbon monoxide (HiPCO) preparation] were suspended with the single-stranded DNA (ssDNA) oligonucleotide $(TAT)_6$ modified at the 3′ end with a primary amine functional group, via ultrasonication. The nanotube suspensions were purified by ultracentrifugation to remove bundles, and excess DNA was removed by centrifugal filtration. The DNA-SWCNT complexes were then conjugated via carbodiimide cross-linker chemistry to a goat polyclonal anti-HE4 immunoglobulin G (IgG) antibody (C-12, Santa Cruz Biotechnology) and subsequently dialyzed against water for 48 hours to remove unreacted reagents. Dynamic light scattering of the dialyzed suspensions indicated a larger size after conjugation with the antibody, confirming that the antibody successfully bound to the DNA-SWCNT complexes (Fig. 1B). Electrophoretic light scattering further suggested successful attachment by an increase in ζ-potential of the DNA-SWCNT complexes after conjugation to the antibody (Fig. 1C), as expected from analogous works (*29*). The stability of the complexes and preservation of nanotube optical properties were confirmed by absorbance and PL excitation/emission spectroscopy (Fig. 1D). All nanotube species (chiralities) exhibited a red shift in emission wavelength (red shift) after antibody conjugation (table S1), suggesting an increase in the local electrostatic charge or increased polarity/dielectric constant of the environment in the immediate vicinity of the nanotube (*26*, *30*).

We assessed the sensitivity and kinetics of the optical response of the Ab-DNA-SWCNT complexes to HE4. The complexes were passivated by incubating with bovine serum albumin (BSA) (*31*) and subjected to testing with recombinant HE4 antigen in 10% fetal bovine serum (FBS), a complex protein environment. The complexes were excited at 730 nm, and the emission was collected across the NIR range of 900 to 1400 nm to simultaneously assess several nanotube chiralities (see Materials and Methods) (*32*). The nanotube emission responded to increasing concentrations of HE4 via monotonic blue shifting of the (9,4) nanotube chirality, with a detection limit of 10 nM and sensitivity of up to 500 nM (Fig. 1E and fig. S1A), as well as the other two chiralities we investigated (fig. S1, B and C). This detection limit is within the range found in ovarian cancer patient serum and ascites (*14*, *33*) of approximately 10 nM and in uterine washings, where median values are 23-fold higher than serum values (~230 nM) (*15*, *16*).

We investigated the specificity of the response of the Ab-DNA-SWCNT complex to HE4 (Fig. 1F). The complex was interrogated with 500 nM HE4 or 500 nM each of nontarget proteins, including urokinase plasminogen activator (uPA), the ovarian cancer biomarker CA-125, and BSA, in addition to 93% FBS. High concentrations, much greater than those found under normal physiological conditions for individual proteins, were chosen to assess for nonspecific interactions. We found either no change or a moderate red shift in the sensor response to each interferent protein condition compared to the control (no protein). The responses were measured transiently, and no further changes were found for 120 min (fig. S1D). When ssDNA-suspended nanotubes in the absence of a conjugated antibody were challenged with HE4, no wavelength shifting response was observed, indicating that the ssDNA-suspended nanotubes did not exhibit an intrinsic response to HE4 (fig. S1E).

We assessed the kinetics of the response of the Ab-DNA-SWCNT complexes to HE4. The complexes exhibited an immediate change in wavelength after introducing HE4, which was detectable after 1 min (Fig. 1G). The signal stabilized by approximately 60 min after HE4 addition. To investigate long-term sensor functionality under simulated in vivo conditions, we incubated Ab-DNA-SWCNT complexes in FBS at 37°C for up to 7 days. When interrogated with HE4, we observed the usual blue-shifting response for 3 days, although at 7 days, the sensor response was significantly changed, wherein a larger response and greater variability were observed (fig. S1F).

The sensor blue shift is likely caused by the removal of water from the surface of the nanotube following the high affinity–specific interaction of HE4 with the antibody. When this binding occurs, we hypothesize that the HE4 protein is brought near to the nanotube surface, displacing water from the surface of the nanotube and thereby reducing the local dielectric constant, causing a blue shift (*28*, *30*). The red shift in response to certain nontarget proteins is likely due to electrostatic interactions of the proteins with the surface of the nanotube that are not strong enough to displace water, causing an increase in the local electrostatic charge environment of the nanotube (*26*, *30*).

We developed a surface-based hyperspectral imaging assay to assess the response of single nanosensor complexes to HE4 in the presence of a minimal amount of patient sample. Ab-DNA-SWCNT complexes were adsorbed to a glass surface and imaged using a near infrared (NIR) hyperspectral microscope to rapidly acquire the spatially resolved spectra from hundreds of individual complexes (Fig. 2, A and B) (*34*–*36*). Baseline hyperspectral cubes were obtained from single nanotubes immersed in phosphate-buffered saline (PBS), resulting in spectra for each complex. Spectra were then acquired from the same imaging field 10 min after spiking a final concentration of 10 nM HE4 into the buffer. The mean blue shift was 1.2 nm [$P = 0.04$, measured for the (8,6) species; Fig. 2C and fig. S2, A and B]. Further, we observed a blue shift of 0.8 nm after spiking in a final concentration of 2.5 nM HE4, but no change after the addition of 1 nM (fig. S2B), denoting a detection limit in this range. In response to 10% FBS, the mean sensor red shift was 2.3 nm ($P = 0.03$; Fig. 2C).

We investigated the individual nanosensor response upon exposure to biofluid samples collected from ovarian cancer patients. The hyperspectral imaging assay allowed measurements of patient samples in volumes as little as 10 μl. Upon exposing the sensor to serum collected from patients diagnosed in the clinic with HGSC or noncancerous, benign conditions, we observed a distinct separation in signal response (Fig. 2D). The HGSC patient serum caused a blue shift of approximately 0.36 nm [SD = 0.16 nm, measured for the (8,6) nanotube species], whereas serum from patients with benign conditions red-shifted the sensors by approximately 1.4 nm (SD = 0.72 nm), resulting in a significant difference between the two cohorts ($P = 0.015$). Using an enzyme-linked immunosorbant assay (ELISA), we measured HE4 concentrations within 0.44 to 0.58 nM in patients with benign conditions and 2.2 to 2.6 nM for HGSC patients. The nanosensor also differentiated between HGSC patient ascites and benign patient peritoneal fluid collected from patients without cancer (Fig. 2E). Peritoneal fluid from benign controls elicited an average red shift of 0.96 nm (SD = 0.64 nm), whereas ascites from HGSC patients caused an average blue shift of 0.27 nm (SD = 0.08 nm), resulting in a significant difference between the two populations ($P = 0.030$). The HE4 concentrations measured by ELISA were 0.86 to 1.1 nM for peritoneal fluid

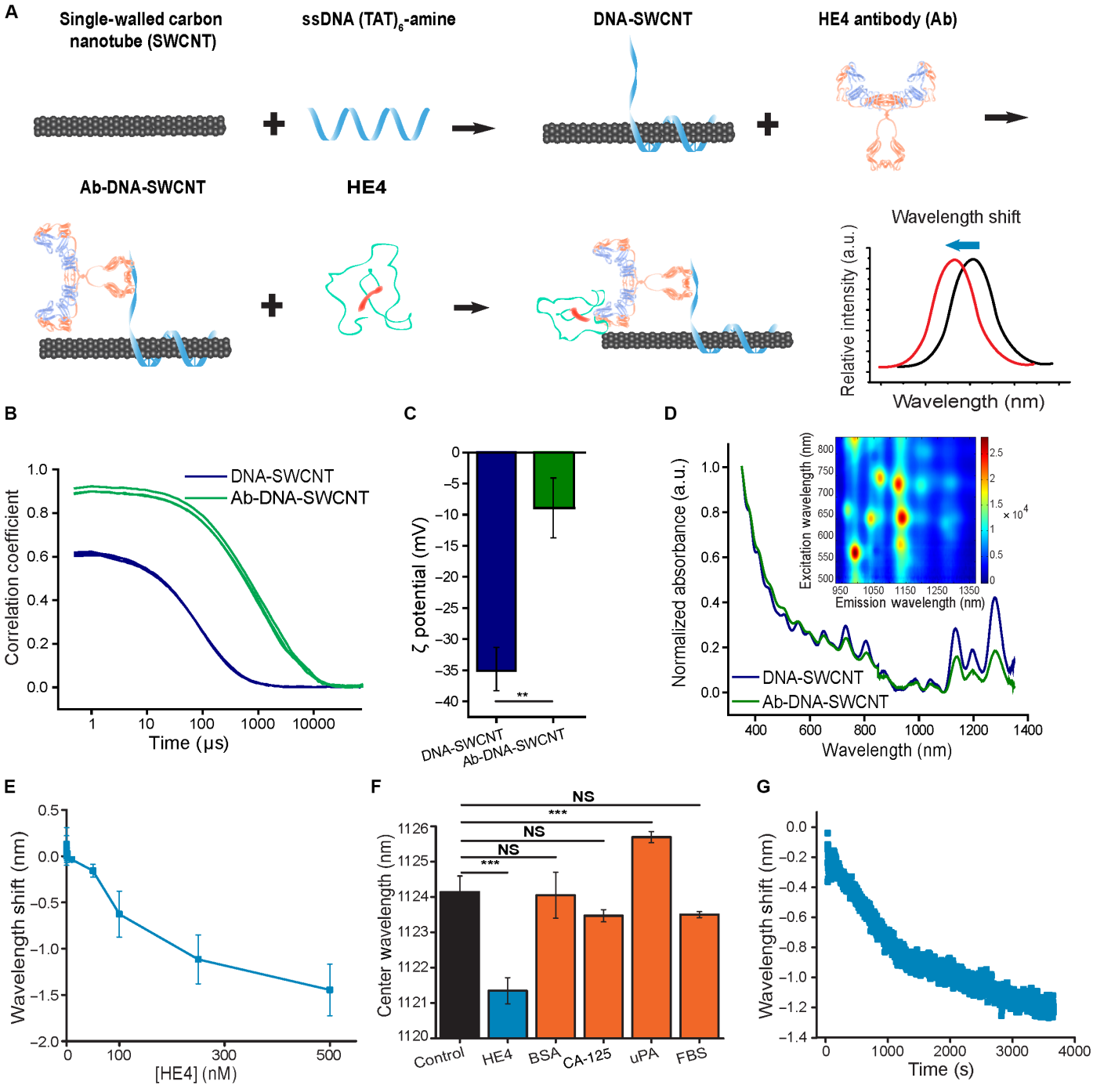

Fig. 1. Design and in vitro characterization of optical nanosensor for HE4. (**A**) Scheme of Ab-DNA-SWCNT complex synthesis and proposed nanosensor function. a.u., arbitrary units. (**B**) Correlograms from a dynamic light scattering instrument showing correlation coefficient of pre-Ab– and post-Ab–conjugated ssDNA-SWCNT samples. $n = 3$ for each complex. (**C**) Electrophoretic light scattering of ssDNA-SWCNT before and after anti-HE4 antibody conjugation. $n = 3$, mean ± SD; $^{**}P < 0.01$, t test. (**D**) Representative absorbance spectra of the hybridized ssDNA-SWCNT before and after conjugation of the anti-HE4 antibody. Inset: Representative PL excitation/emission plot of the Ab-DNA-SWCNT sensor. (**E**) Dose-response curve of the Ab-DNA-SWCNT sensor emission [of the (9,4) nanotube species] as a function of HE4 concentration in 10% fetal bovine serum (FBS). Each point is the mean of three experiments ± SD. (**F**) Response of the Ab-DNA-SWCNT complex to interferent proteins. $n = 3$, mean ± SD; control and HE4, $P = 1.0 \times 10^{-4}$; control and bovine serum albumin (BSA), $P = 0.998$; control and CA-125, $P = 0.163$; control and urokinase plasminogen activator (uPA), $P = 1.0 \times 10^{-3}$; control and FBS, $P = 0.64$ [two-sided one-way analysis of variance (ANOVA) with Dunnett's post hoc analysis]. NS, not significant. (**G**) Representative kinetic response of nanotube emission upon introducing recombinant HE4.

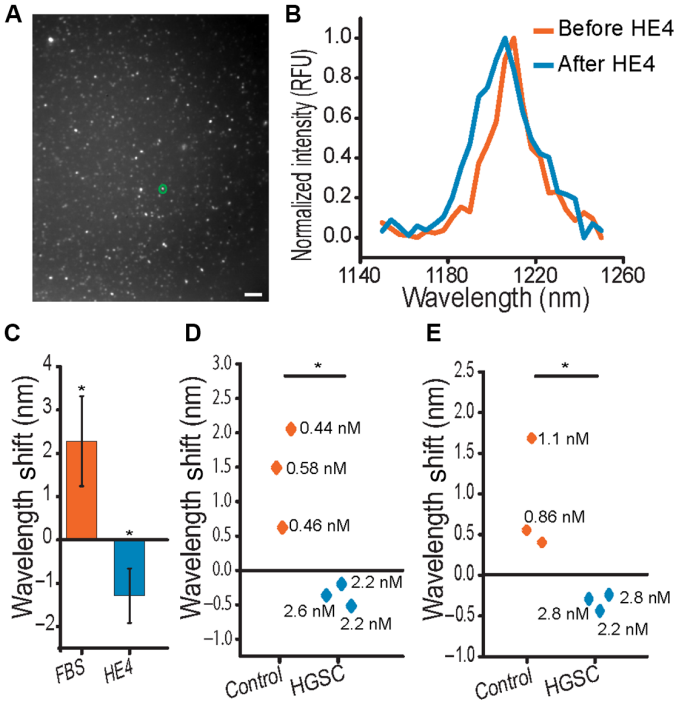

Fig. 2. Single-sensor HE4 measurements in patient biofluids. (**A**) NIR image of Ab-DNA-SWCNT complexes adsorbed to a glass surface. Scale bar, 5 μm. (**B**) Representative spectra of a single complex, denoted by the green circle in (A), before and 10 min after introducing recombinant HE4. RFU, relative fluorescence units. (**C**) Shift in sensor emission wavelength 10 min after addition of recombinant HE4 or 10% FBS. Pre- to post-FBS, $^{*}P = 0.03$; pre-HE4 to post-HE4, $^{*}P = 0.04$ (two-sided *t* test). $n = 82$ single nanotubes before and 98 after FBS, 100 before HE4, and 97 after HE4. Data shown are means ± SEM. (**D**) Sensor response to serum. $n = 3$ HGSC patients or patients with benign conditions. HE4 concentrations, measured independently via enzyme-linked immunosorbent assay (ELISA), are specified for each sample. $^{*}P = 0.015$, two-sided *t* test. (**E**) Sensor response to HGSC patient ascites or peritoneal fluid from patients with benign conditions. $n = 3$. HE4 concentrations, measured independently via ELISA, are specified for each sample, with one exception due to sample volume limitation. $^{*}P = 0.03$, two-sided *t* test.

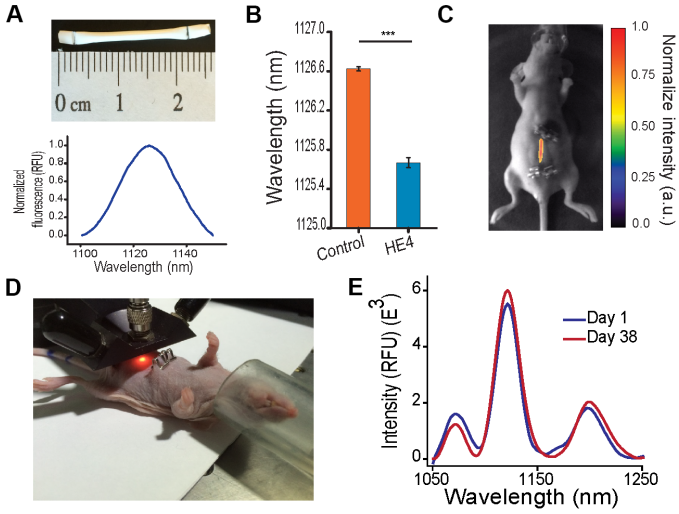

Fig. 3. Implantable nanosensor device. (**A**) Semipermeable 500-kDa MWCO membrane capillary incorporating Ab-DNA-SWCNT complexes. Spectrum of the nanosensor acquired through the capillary wall. (**B**) Emission wavelength from the sensor after introducing recombinant HE4. $n = 3$, mean ± SD; $^{***}P = 7.2 \times 10^{-6}$, two-sided *t* test. (**C**) NIR image of nanosensor emission from the implanted device, overlaid onto a reflected light image of the mouse. (**D**) Photograph of typical data acquisition from the probe-based system used to excite/acquire NIR emission from the implanted sensor in mice. (**E**) Representative NIR fluorescence spectra of sensors implanted into healthy mice and measured 1 hour and 38 days after implantation.

from patients with benign conditions and 2.2 to 2.8 nM for HGSC patient ascites. The HE4 concentrations in noncancerous serum and peritoneal fluid samples are consistent with the upper range of various benign conditions, with HE4 levels greater than that of normal individuals, whereas the HGSC serum and ascites samples are consistent with the upper range of HGSC patient samples (*37*, *38*). Because all benign serum and peritoneal fluid samples contained less than 1.1 nM HE4 and all HGSC patient fluids contained 2.2 to 2.8 nM HE4, these results confirm the detection limit of between 1 and 2.5 nM HE4 using the surface-based nanosensor assay and the ability to differentiate HGSC patient from benign fluids ex vivo.

To assess the function of the nanosensor in vivo, we developed a membrane-based device to implant the Ab-DNA-SWCNT complexes into live mice. The complexes, passivated with BSA, were loaded into a semipermeable polyvinylidene fluoride (PVDF) membrane capillary with a molecular weight cutoff (MWCO) of 500 kDa. We chose this MWCO to be larger than the HE4 antigen (approximately 25 kDa) but smaller than the sensor complex. We estimated the mass of the complex, assuming that an average diameter nanotube is 1.0 nm, the experimentally determined average length is 166 nm (*26*), and the derived ssDNA-to-nanotube weight ratio from simulations is 1:1 (*39*), to be 1446 kDa (see the Supplementary Text). The material allowed excitation/emission of nanotubes through the membrane (Fig. 3A). We first tested the response of the implantable sensor device immersed in 10% FBS, resulting in a 1-nm blue shift upon exposure to 100 nM recombinant HE4 after 60 min, as compared to controls ($P = 7.2 \times 10^{-6}$; Fig. 3B).

We developed a minor surgical method to investigate the functionality of the implantable sensor in vivo. The membrane-encapsulated sensors were surgically implanted into healthy, 4- to 8-week-old female athymic nude mice (Envigo Hsd:Athymic Nude-*Foxn1*^{nu}) under anesthesia (fig. S3; see Materials and Methods). The implants were sutured within the peritoneal cavity to the interior of the parietal peritoneum medially above the intestines, and the overlying skin was clipped closed. Placement of the implantable device and nanosensor emission from within the peritoneal cavity were confirmed by whole-animal NIR imaging (Fig. 3C). Typical results revealed bright emission medially to the abdomen and no nanotube leakage from the membrane. Following implantation, mice were allowed to become alert and ambulatory, exhibiting no adverse effects or signs of distress from surgery or the implanted device.

We developed instrumentation to noninvasively acquire spectra from the sensor and assess its response in vivo. A fiber optic probe–based system was used to excite an area of approximately 0.8 cm^2 with a 730-nm laser (see Materials and Methods). Emission from the sensor was collected through the same fiber bundle, which was coupled to a spectrometer/NIR array detector. Spectra were obtained from mice reanesthetized after sensor implantation. Spectra were acquired with a 3 s integration time by placing the probe approximately 1 to 2 cm above the mouse skin. Three measurements were taken and averaged per mouse (Fig. 3D). The distance through the skin and peritoneum was

approximately 2 mm of tissue. To confirm the stability of the nanosensor, the implantable device, and its long-term optical functionality in vivo, a mouse was implanted with the sensor. Fluorescence was measured 60 min and 38 days following injection (Fig. 3E). The results suggest long-term stability of the emission of the sensor implant.

We investigated the response of the implanted sensor when challenged with exogenous recombinant HE4. Implanted mice were intraperitoneally injected with 10 pmol of HE4, an equal amount of BSA, or left untreated (n = 3). Sensor fluorescence was obtained as above with the fiber optic probe–based system. Three measurements were taken per mouse per time point, baseline-subtracted (fig. S4), and fit using a Lorentzian function to obtain the emission center wavelength. The sensor implants were measured before implantation; in vivo following implantation but before injection; 15 min and 1, 2, 4, and 24 hours after injection; and ex vivo after explantation (fig. S5, A to H). The sensors exhibited a distinct blue-shifting response by 15 min after HE4 injection, which stabilized by 60 min (Fig. 4A and fig. S5, I and J), comparable to the in vitro kinetics data. Alternatively, mice injected with BSA exhibited a slight red shift or no change in emission wavelength throughout the experiment. At 60 min, the implanted sensor in the HE4-injected mice exhibited a 0.7-nm blue shift, as compared to controls (Fig. 4B)—almost identical to the magnitude observed in vitro upon interrogating with the same quantity of HE4 (0.6-nm blue shift; Fig. 1B). This change was significantly different when compared to the change in center wavelength of the sensor in mice injected with BSA (P = 0.016). Following sacrifice, the sensor device was removed and was found to exhibit no compromise in structural integrity or function.

We next investigated the in vivo sensor response to tumor-derived HE4 within orthotopic murine models of ovarian cancer. Four cohorts of athymic nude mice were injected intraperitoneally with approximately 10 million cells of four different luciferase-expressing cell lines: OVCAR-3, SK-OV-3, OVCAR-5, and OVCAR-8 (n = 4 of each). The OVCAR-3 and OVCAR-5 cells express high levels of HE4, whereas SK-OV-3 and OVCAR-8 cells express low to negligible levels of HE4 (*11*). These cell lines are thought to represent HGSC with the exception of SK-OV-3, which is likely not of HGSC origin (*40*). We confirmed HE4 expression in OVCAR-3 and OVCAR-5 and a lack thereof in SK-OV-3 and OVCAR-8 cells via ELISA on conditioned cell culture media (table S2). Tumors were allowed to grow for approximately 4 weeks, after which in vivo bioluminescence imaging showed significant tumor burden in the mice (Fig. 4C). Mice exhibited distended, fluid-filled abdomens typical of ovarian cancer–associated ascites and solid tumor nodules in the peritoneal cavity. The presence of HE4 in OVCAR-3 and OVCAR-5 ascites and negligible concentrations or absence of HE4 in SK-OV-3 and OVCAR-8 ascites were confirmed via ELISA on ascites drawn or flushed from the peritoneal cavity (table S2). Tumor burden was further confirmed via hematoxylin and eosin (H&E) staining on resected tumor nodules (fig. S6).

To measure HE4 in ovarian cancer–bearing mice using the nanosensor, the devices were implanted into the peritoneal cavity following initial spectral characterization (fig. S7A). Surgical implantation was performed as described above on mice 4 weeks after tumor cell injection. Nanosensor emission was measured in the tumor-bearing mice in vivo using the optical probe system (Fig. 4D) for 24 hours. The sensors were also interrogated after sacrifice and explantation at 24 hours (fig. S7, B to G). Three measurements were taken per mouse per time point and baseline-subtracted. The spectra were then fit with Lorentzian functions to record the emission center wavelength. The implanted sensors exhibited an immediate blue shift response in mice bearing HE4-expressing tumors within 15 min that stabilized by 60 min (Fig. 4E and fig. S7, H and I), similar to the in vitro results (Fig. 1G). Similar to the exogenous protein injection experiments, the sensors in mice bearing HE4 nonexpressing tumors exhibited no wavelength changes or slight red shifting. At 60 min, in mice bearing OVCAR-3 or OVCAR-5 cells, the sensor exhibited a 0.91- or 1.2-nm blue shift, respectively, as compared to controls, while it exhibited a negligible change in SK-OV-3 and OVCAR-8 models (Fig. 4F). The mean emission wavelength of the sensor from each HE4 (−) mouse was significantly different from that of each HE4 (+) mouse. Emission was bright and stable across all measurements (fig. S8A). Following mouse sacrifice and sensor explantation,

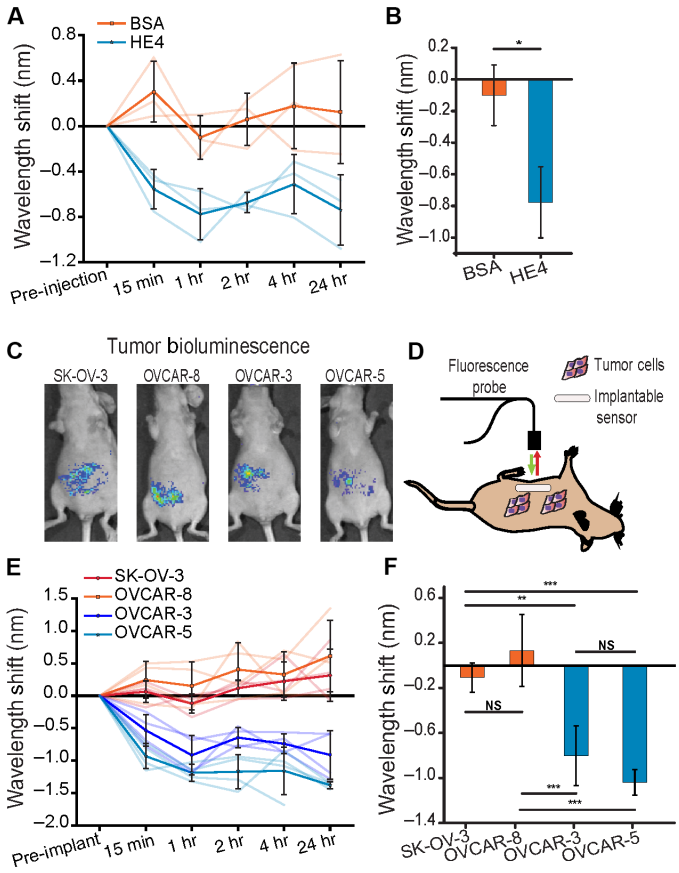

Fig. 4. In vivo measurement of HE4 in orthotopic ovarian cancer models. (**A**) Change in emission center wavelength in mice following intraperitoneal injection of 10 pmol of BSA or HE4, compared to emission in uninjected mice. Bold lines represent mean ± SD. n = 3. Lighter lines represent measurements from each mouse. (**B**) Change in emission center wavelength at 60 min after injection of BSA or HE4 compared to uninjected mice. n = 3, mean ± SD; *P = 0.016, two-sided t test. (**C**) Representative bioluminescence images denoting tumor burden in the peritoneal cavity of nude mice inoculated with luciferase-expressing cell lines. (**D**) Schematic method of HE4 measurement in live tumor-bearing mice. (**E**) Change in sensor emission center wavelength following implantation into mice bearing four different orthotopic intraperitoneal tumor models. Bold lines represent mean ± SD. n = 4. Lighter lines represent traces from the emission within each mouse. (**F**) Sensor response from all mice at 60 min after implantation. n = 4, mean ± SD. Sensor wavelength difference between models and statistical analysis: SK-OV-3 and OVCAR-3 (0.79 nm; $P = 4.4 \times 10^{-3}$), SK-OV-3 and OVCAR-5 (1.07 nm; $P = 3.9 \times 10^{-4}$), OVCAR-8 and OVCAR-3 (1.07 nm; $P = 3.9 \times 10^{-4}$), OVCAR-8 and OVCAR-5 (1.34 nm; $P = 4.5 \times 10^{-5}$), SK-OV-3 and OVCAR-8 (0.27 nm; P = 0.46), and OVCAR-3 and OVCAR-5 (0.27 nm; P = 0.48) by two-sided one-way ANOVA with Tukey's post hoc analysis.

we found that the blue shift remained consistent when the sensor was interrogated using the optical probe (fig. S8B).

DISCUSSION

This work describes in vivo optical quantification of a soluble cancer protein biomarker and direct correlation with disease state using an implanted optical sensor with carbon nanotubes as the transduction element. Many imaging modalities that visualize tumors by binding protein targets exist (*41*). In addition, previous work using carbon nanotube electrical (*42*) and optical properties has produced sensors for the detection of proteins in vitro, including a chip-based optical sensor to measure the cardiovascular disease biomarker cardiac troponin T (*43*) and an in vivo sensor for the small-molecule inflammatory biomarker nitric oxide (*27*).

The current work described the construction and characterization of a carbon nanotube–based optical sensor for the ovarian cancer protein biomarker HE4. We found that the sensor can quantify HE4 in patient serum and ascites samples at relevant biomarker concentrations, potentiating future use as a rapid or point-of-care sensor. Finally, we developed, characterized, and used an implantable device in the peritoneal cavity of four murine models of ovarian cancer to detect the HE4 biomarker and differentiate biomarker-producing murine ovarian cancer models from non–biomarker-producing models.

The application of this sensor technology in the clinic will obviously require multiple follow-up studies. Data presented herein show wavelength shifting responses of up to 2 nm. Although consistent and reproducible, there was some minor variation in values across experiments and in initial emission wavelengths before detection. We note that this is likely due to the different nanotube local environments across varying platforms, including in solution, on a solid surface, and within a membrane in live mice (*34*). Minor variability in initial center wavelength measurements was addressed by performing spectral characterization of each sensor before implantation. We also found slight differences in the detection limit when used in solution versus on a glass surface. However, future work will investigate several approaches to producing a larger spectral change and thereby improve sensitivity of both ex vivo measurements of patient biofluids and in vivo detection, including separating nanotube chiralities to decrease spectral overlap and heterogeneity in emission center wavelengths (*39*, *44*), performing site-directed antibody conjugation chemistry to increase proper antibody orientation (*45*), increasing the total number of antigen-binding events using multivalent polymers (*32*), and modifying polymers to exacerbate the magnitude of the shift (*28*). In addition, carbon nanotubes with higher quantum yields would allow for greater tissue penetration of the optical signal.

The long-term function of the implant will be important for most applications of this technology. Herein, we demonstrated stable sensor function in vivo up to 24 hours and consistent emission intensity in vivo over 38 days, although in vivo sensor functionality over extended periods requires further investigation. Should antibody stability be an issue, more stable antibody constructs, such as single-chain variants or nanobodies (*46*, *47*) or other sensing elements such as aptamers, (*48*, *49*) may be investigated. Regarding the implant housing material, it is known that PVDF in general and the specific implant used here is highly biocompatible (*50*) and has been used in immunocompetent mice and rats, finding no immune reactions caused by the membranes (*51*). However, to modulate any potential biofouling or biocompatibility issues, it is possible to coat the membrane with polyethylene glycol or other antifouling materials (*52*). Alternatively, the nanosensors may be embedded directly in a hydrogel matrix, as has been investigated with carbon nanotubes in vivo, finding no local inflammation (*27*). Further, although we expect no exposure of the nanosensor complex when immobilized in the implant device, well-dispersed, purified SWCNTs such as those used here do not exhibit any immunogenic or toxic effects (*36*, *53*).

Concerning the form factor and site of implantation of a clinical device for detection of ovarian cancer biomarkers, several options may be considered. Detection proximal to disease sites will increase the likelihood that the sensor will be exposed to higher levels of HE4 in the presence of cancer. It is unlikely that implantation of this sensor into the peritoneal cavity would yield diagnostic value due to poor biomarker differentiation at that location (*38*). However, potential locations include areas near the ovaries, fallopian tube, or within the uterine cavity where HE4 is expressed up to 12-fold higher in patients with ovarian cancer compared to benign conditions and up to 23-fold higher than in the serum (*15*, *16*). Devices such as T-shaped birth control intrauterine devices (IUDs) are approximately 3 cm in each planar dimension (*54*). Because our implantable device is roughly the same size, it may be inserted into the uterine cavity in a similar manner to existing IUDs or in the fallopian tubes endoscopically, wherein nanotube fluorescence could easily be probed endoscopically or through the body. Depending on the patient, it may be possible to obtain measurements using a similar probe-based device external to the patient; however, in certain circumstances, endoscopic probe-based measurements may be necessary. Although there is potential invasiveness and associated risk with these procedures, these would likely be acceptable in light of the potential diagnostic benefits.

The stratification of patients to determine who may be good candidates will be important for the successful translation of this technology. Current evidence shows up to 23-fold greater uterine cavity concentrations of HE4 compared to serum concentrations and that these levels are associated with disease status (*15*, *16*). Although this portends early-stage disease screening, additional studies are warranted to modify and assess the technology described here for use in a clinical context. Risk factors that are indicative of an increased risk for ovarian cancer include family history of ovarian or breast cancer, patients with *BRCA1* or *BRCA2* mutations (*55*), and individuals experiencing early menarche, late menopause, or endometriosis (*56*). These patients may be appropriate for sensor implantation between the ages of 30 and 40 if longitudinal monitoring (*57*) over a period of months to years can be achieved. In addition, patients who have been diagnosed and treated for primary disease may be appropriate to monitor for recurrence. Most patients treated for advanced ovarian cancer initially respond to first-line therapy and then subsequently relapse (*58*). Thus, careful monitoring after the completion of treatment may allow for a more rapid determination of whether the disease is returning after initial therapy, alerting physicians earlier to the need to initiate a new therapeutic approach or consider additional surgical cytoreduction.

Regarding the choice of protein biomarker to measure using a clinical device, several issues must be considered. We focused herein on HE4, which, in the context of patient serum-based measurements for ovarian cancer, has shown some utility for clinical diagnosis and, in some circumstances, more so than the more commonly used CA-125 (*12*, *13*), although not in all circumstances (*59*). Other proteins, including YKL-40 and mesothelin, have additionally been found to exhibit elevated levels in the uterine cavities of patients with ovarian cancer (*15*, *16*). It may be desirable to simultaneously measure multiple biomarkers to potentially afford increased specificity for and sensitivity to disease. To develop a single device for multiplexed detection (*28*), one may use either physical

separation (*60*) of elements sensitive to different biomarkers on the same device or chirality separation of carbon nanotubes (*39*, *44*) to enable different nanotube species to be engineered to detect different biomarkers and measured individually via spectral separation of emission bands.

CONCLUSION

We developed an implantable nanosensor to noninvasively detect an ovarian cancer biomarker produced in a localized region within the body and transmitted via NIR emission to an external detector. The sensor used SWCNTs to transduce the binding of HE4 to an immobilized antibody via modulation of the intrinsic NIR emission of the nanotubes. The nanotube-antibody complexes detected HE4 in serum and ascites from ovarian cancer patients. The nanotube complexes were then loaded into a semipermeable membrane to result in an implantable device that could be probed noninvasively in vivo. The sensors quantified exogenously derived HE4 and detected endogenous HE4 in orthotopic murine models of ovarian cancer to differentiate HE4-producing models from biomarker-deficient models. The work portends clinical translation of implantable devices for use in patients with risk factors for disease to detect disease onset, recurrence, or to monitor treatment response.

MATERIALS AND METHODS

Sensor synthesis

The HE4 sensor complex was synthesized by probe-tip ultrasonication of as-prepared HiPCO SWCNTs (Unidym) with amino-modified ssDNA oligonucleotide with the sequence 5′-TATTATTATTATTAT-TAT/AmMO/-3′ (Integrated DNA Technologies), under previously described conditions (*34*). Briefly, a 2:1 mass ratio of ssDNA to dried nanotubes was added to 1 ml of 1X PBS and sonicated for 30 min at 40% of the maximum amplitude (~13 W; Sonics & Materials Inc.). The suspensions were then ultracentrifuged (Sorvall Discovery 90SE) for 30 min at 280,000*g*. The top 75% of the solution was removed for further processing, discarding the bottom 25% that contained unsuspended nanotubes and carbonaceous material. Amicon centrifugal filters with a 100-kDa MWCO were used (Millipore) to remove free ssDNA and to concentrate the samples, which were resuspended in 1X PBS. Absorbance spectra were obtained with a ultraviolet/visible/near-infrared (UV/Vis/nIR) spectrophotometer (Jasco V-670) to determine sample concentration using the extinction coefficient Abs_{630} = 0.036 liters mg^{-1} cm^{-1}.

The resulting DNA-SWCNT complex was then chemically conjugated via carbodiimide chemistry to goat polyclonal anti-HE4 IgG antibody (C-12, Santa Cruz Biotechnology) to form the Ab-DNA-SWCNT sensor construct. The carboxylic acids of the antibody were first activated with 1-ethyl-3-(3-dimethylainopropyl)carbodiimide and *N*-hydroxysuccinimide for 15 min. This reaction was quenched with 1.4 μl of 2-mercaptoethanol. The activated antibody was added in an equimolar ratio to the ssDNA. Following 2 hours of incubation on ice, the conjugate was dialyzed against water with a 1-MDa MWCO filter (Float-A-Lyzer G2; Spectrum Labs) at 4°C for 48 hours with two buffer changes to remove unconjugated antibody and reaction reagents.

NIR spectroscopy and imaging experiments

NIR fluorescence emission spectra from antibody-conjugated and unconjugated nanotubes in solution were acquired using a home-built optical setup (*32*). This apparatus consists of a SuperK EXTREME supercontinuum tunable white light laser source (NKT Photonics) with a VARIA tunable bandpass filter to modulate the output within the 500- to 825-nm range. A bandwidth of 20 nm was used. Alternatively, a 1-W continuous-wave 730-nm laser source (Frankfurt Laser Company) was used. The light path was shaped and fed into the back of an inverted IX-71 microscope (Olympus) and passed through a 20× NIR objective (Olympus) to illuminate a 100-μl sample in a UV half-area 96-well plate (Corning). Emission was collected back through the 20× objective and passed through an 875-nm dichroic mirror (Semrock). The light was f/# matched to the spectrometer using glass lenses and injected into an IsoPlane spectrograph (Princeton Instruments) with a 410-μm slit width. The emission was dispersed using a 86 g/mm grating with blaze wavelength of 950 nm. The spectral range was 930 to 1369 nm with a resolution of ~0.7 nm. The light was collected by a PIoNIR InGaAs 640 × 512 pixel array (Princeton Instruments). Single spectra were acquired using the 730-nm laser or the supercontinuum laser source with the variable bandpass filter centered at 730 nm. Excitation/emission plots, also dubbed PL plots, were compiled using the supercontinuum laser for excitation. Spectra were acquired between movements of the VARIA bandpass filter in 3-nm steps from 500 to 827 nm. An HL-3-CAL EXT halogen calibration light source (Ocean Optics) was used to correct for wavelength-dependent features in the emission intensity arising from the excitation power, spectrometer, detector, and other optics, as previously described (*26*). A Hg/Ne pencil-style calibration lamp (Newport) was used to calibrate spectrometer wavelength. Data were obtained from each well at multiple time points using custom LabView (National Instruments) code.

NIR fluorescence images and spectra were obtained from a hyperspectral microscope, as previously described (Photon etc.) (*34*). Briefly, the setup consists of an inverted IX-71 microscope (Olympus). Experiments were performed with a continuous-wave 2-W 730-nm laser (Frankfurt) fed through a 100× oil immersion lens (Olympus). Nanotube samples immobilized on a glass surface were excited, and emission was collected through the objective. To obtain spectra, light was fed through a volume Bragg grating to obtain images in sequential 4-nm steps from 900 to 1400 nm (hyperspectral cubes). Light was collected using a 256 × 320 pixel InGaAs array.

Individual NIR fluorescence spectra from implantable membranes in vivo and ex vivo were obtained using a home-built preclinical fiber-optic probe spectroscopy system. A continuous-wave 1-W 730-nm laser (Frankfurt) was injected into a bifurcated fiber optic reflection probe bundle. The bundle consisted of a 200-μm, 0.22 numerical aperture (NA) fiber optic cable for sample excitation located in the center of six 200-μm, 0.22 NA fibers for collection. Long-pass filters were used to block emission below 1050 nm. The light was focused into a 303-mm focal length Czerny-Turner spectrograph (Shamrock 303i, Andor) with the slit width set at 410 μm. Light was dispersed by a 85 g/mm grating with blaze wavelength of 1350 nm and collected with an iDus InGaAs camera (Andor).

Live animal NIR images were obtained using a preclinical NIR imaging apparatus consisting of a two-dimensional InGaAs array and two 2-W 730-nm lasers (Photon etc.). The mouse was anesthetized with 1 to 3% isoflurane administered via nose cone during imaging. A 1100-nm long-pass filter was placed into the emission path to reduce autofluorescence. The background-subtracted NIR fluorescence image was overlaid on an image of the mouse taken under ambient visible light.

In vitro sensor characterization

Absorbance spectra of the Ab-DNA-SWCNT complex were obtained with a UV/Vis/NIR spectrophotometer, as described above. PL plots

and individual spectra were obtained from the antibody-conjugated and unconjugated nanotubes using a home-built microscopy apparatus, as described above. PL plots were obtained from the antibody-conjugated sensor and unconjugated control to determine the effect on each nanotube chirality of antibody conjugation. Individual spectra were obtained from samples using the 730-nm laser.

To test sensor response to HE4, the Ab-DNA-SWCNT complex was first incubated on ice with a 50X BSA/SWCNT ratio to passivate the nanotube surface (*31*). The passivated sensor complex was added to a 96-well plate at a nanotube concentration of 0.25 mg/liter in a 100-µl total volume of PBS and 10% FBS (Gibco). Recombinant human HE4 (Glu31-Phe124, RayBiotech) was added to the sensor complex in separate wells at concentrations of 0 nM (baseline control), 1 pM, 10 pM, 100 pM, 1 nM, 10 nM, 50 nM, 100 nM, 250 nM, and 500 nM. Data were taken for up to 2 hours in 5-min increments. Kinetic response experiments were performed by introducing 500 nM HE4 to the sensor and measuring the emission via NIR spectroscopy every 3 s up to 60 min. To assess sensor response in simulated in vivo conditions, we incubated the sensor in 95% FBS at 37°C for 7 days. Aliquots were removed and interrogated with 50 nM HE4 at 1 hour, 1 day, 3 days, and 7 days via NIR spectroscopy. All experiments were performed in triplicate.

To test sensor specificity, we first incubated the Ab-DNA-SWCNT complex with BSA on ice as above. Passivated sensor complexes were added to a 96-well plate at a nanotube concentration of 0.25 mg/liter in a 100-µl total volume of PBS and 10% FBS. In triplicate, the following were added into wells: 500 nM recombinant human HE4, 500 nM recombinant human uPA [a metastatic cancer biomarker (RayBiotech)], 500 nM native human CA-125 of cellular origin (Cell Sciences), 500 nM BSA (Sigma-Aldrich), or an additional 83% (for a total of 93%) FBS. To ensure specificity of the sensor construct, 500 nM recombinant human HE4 was added to DNA-SWCNT complexes without antibody, as described above. Experiments were performed with the same time points as above.

Ex vivo sensor characterization

The nonpassivated Ab-DNA-SWCNT sensor complex (10 µl) was added to a collagen-coated MatTek (Ashland, MA) glass-bottom dish for 30 s and removed, allowing the complexes to be deposited on the surface. Then, 90 µl of 1X PBS was added to the dish. A single-broadband NIR fluorescence image was obtained in the 900-to-1400-nm range using the hyperspectral microscope described above (*34*) under a laser excitation of 730 nm. A continuous stack of emission wavelength–defined images (hyperspectral cube) was acquired with the volume Bragg grating in place, moving in 4-nm steps between 1150 and 1250 nm. Then, 10 µl (final concentration of 10 nM) of recombinant HE4 was added to the PBS for 10 min before a second cube was acquired. Spectra from 50 to 100 individual nanotubes were processed as described above, and the mean emission wavelength was calculated. A Student's *t* test was used to determine significance between the pre-HE4 and post-HE4 addition populations. A separate experiment was performed for an equal concentration of BSA to test specificity of the response of the sensor in this context.

The immobilized Ab-DNA-SWCNT complexes were interrogated with 10 µl of patient samples. Fluids from three separate patients with each condition were used: benign serum, HGSC serum, benign peritoneal fluid, and HGSC ascites. Each sample was obtained as previously described (*15*, *16*) under the Memorial Sloan Kettering Cancer Center (MSKCC) Institutional Review Board–approved protocols, and informed consent was obtained. A Student's *t* test was performed to compare sensor shift for benign samples and HGSC samples. All patient samples (except one benign peritoneal fluid due to minimal volume obtained) were analyzed by ELISA to quantify HE4 (R&D Systems).

Implantable device development

The Ab-DNA-SWCNT sensor complex was passivated by incubation on ice with BSA in a 50X BSA/SWCNT ratio for 30 min. FBS was then added to reach a 10% concentration. A semipermeable 500-kDa MWCO PVDF KrosFlo dialysis membrane (Spectrum Labs) ~2 mm in diameter was cut 2 to 3 cm long. A volume of 15 to 20 µl of SWCNTs (4 mg/liter; or 60 to 80 ng of the complex) was injected into the capillary. Both ends of the membrane were heat-sealed, leaving a ~2-mm flap on each side.

In vitro characterization of implantable device

The optical response of the Ab-DNA-SWCNT complex within the capillary device was tested by immersing the membrane in 1 ml of 1X PBS and adding 100 nM recombinant HE4 to the solution. NIR emission of the nanotubes inside the membrane was obtained using the home-built microscopy setup, as described above. Spectra were obtained before HE4 addition and every 30 min thereafter. Background subtractions were performed with a blank membrane containing no nanotubes. Fluorescence measurements were taken in triplicate.

Exogenous HE4 detection in vivo

All animal experiments were approved by the Institutional Animal Care and Use Committee at MSKCC. Animal numbers were chosen to ensure repeatability while minimizing animal use. To test in vivo sensor functionality, nine healthy, 4- to 8-week-old female athymic nude mice (Envigo Hsd:Athymic Nude-*Foxn1*^{nu}) were used to implant the membrane into the peritoneal cavity. Separately, one mouse was implanted with the sensor to monitor its long-term stability and fluorescence. Measurements from this mouse were performed at 60 min and 38 days after implantation. Before implantation, NIR fluorescence spectra were acquired from the implant using the fiber optic probe spectroscopy apparatus described above. Surgical implantation and fluorescence spectroscopy were performed under 1 to 3% isoflurane anesthesia, administered via a nose cone. Two ~2-mm incisions were made in the skin and below the parietal peritoneum: one ~5 mm distal to the xiphoid process and one ~2 cm distally of the first incision (fig. S3). The membrane was inserted through the proximal incision through to the distal incision. The flaps at each end of the device were sutured to the parietal peritoneum using 5-0 Monocryl (poliglecaprone 25) absorbable sutures (Ethicon). The skin was clipped twice at each incision with 9-mm stainless steel AutoClips to close the incisions (Mikron Precision Inc.). Between time points, mice were alert and ambulatory, exhibiting no visible signs of pain or distress. NIR fluorescence spectra from the sensor device were acquired using the probe-based system by pointing the fiber probe at the abdomen of the anesthetized mouse from a distance of 1 to 2 cm. Mice were then injected with 10 pmol of HE4 or BSA in 100 µl of PBS, or they were left uninjected as a second control ($n = 3$). NIR spectra were then acquired 15 and 60 min following injection. Spectra were also collected at 2, 4, and 24 hours after injection. Following 24 hours, mice were sacrificed, and the implantable devices were removed. Spectra were again acquired from the device ex vivo. Spectra were processed as described above. The change in emission center wavelength of the implant within a mouse was obtained by subtracting the average center wavelength of the control uninjected mice at the appropriate time point (to control for variability in the sensor due to the in vivo environment) and then the initial preimplant center wavelength for the given mouse

(to control for variability in initial sensor emission) from the emission center wavelength measured at each time point in vivo.

Murine models

Luciferized cell lines OVCAR-3 [cultured in RPMI-1640 + 20% FBS + insulin (0.01 mg/ml; Humulin R, Lilly) + Primocin (100 μg/ml; InvivoGen)], SK-OV-3 (cultured in Dulbecco's modified Eagle's medium low glucose + 10% FBS + Primocin; American Type Culture Collection), OVCAR-5, and OVCAR-8 (both cultured in RPMI-1640 + 1 mM sodium pyruvate + 10% FBS + Primocin) were grown at 37°C under humid conditions. All culture reagents were from Gibco unless otherwise noted. Cells were passaged at 80 to 90% confluency approximately once weekly, and media was changed every 2 to 3 days. ELISA was performed to determine the presence of HE4 in conditioned culture media collected at ~90% confluency (R&D Systems). Upon reaching near confluency, cells were trypsinized for 10 min at 37°C, complete media was added to deactivate trypsin, cells were centrifuged at 150*g* for 7 min at 4°C, and pellets were resuspended in cold 1X PBS. Cells were counted using a Tali image-based cytometer (Invitrogen). Approximately 10 million cells in a 100-μl volume were injected intraperitoneally into four to eight female athymic nude mice ($n = 4$) (Envigo). Mice were housed under standard conditions, and whole-animal bioluminescence imaging was performed twice weekly to monitor cell proliferation using the IVIS Spectrum In Vivo Imaging System (Perkin Elmer; Fig. 4C) using standard firefly luciferase bioluminescence settings. Approximately 4 to 5 weeks following injection, maximal bioluminescence signal was obtained, and most mice exhibited distended, fluid-filled abdomens typical of peritoneal ascites with some solid tumor nodules.

In vivo studies with implantable sensor device

Before implantation, NIR spectra were acquired from the sensor devices using the probe-based spectroscopy system. Sensor devices were implanted into each mouse, as described above, with care taken to minimize loss of ascitic fluid. Spectra were obtained at 15 min, 1 hour, 2 hours, 4 hours, and 24 hours following implantation. After 24 hours, mice were sacrificed, the implant devices were removed, and spectra of the devices were acquired. The change in emission center wavelength of the implant within a mouse at a given time point was obtained by subtracting the average center wavelength of control uninjected mice at the appropriate time point (to control for variability in the sensor due to the in vivo environment), and then, the initial preimplant center wavelength for the given mouse (to control for variability in initial sensor emission) from the emission center wavelength was measured at each time point in vivo. Upon sacrificing the mice, ascitic fluid was removed directly from the peritoneal cavity of the mice with a needle and syringe or washed with up to 2 ml of 1X PBS and removed. Solid tumor nodules were removed for histological analysis.

An ELISA was performed using an HE4 kit (R&D Systems) to quantify HE4 mouse in ascites. Tumor tissues were fixed in 4% paraformaldehyde (PFA), dehydrated, and paraffin-embedded before 5-μm sections were placed on glass slides. The paraffin was removed and slides were stained with H&E for basic histological analysis.

Statistical analysis and spectral fitting

Zeta potential, surface-based, in vitro confirmation of implantable device sensitivity to HE4, and in vivo protein injection experiments were analyzed by two-sided *t* tests. In vitro specificity experiments were analyzed by a two-sided one-way ANOVA with Dunnett's post hoc analysis to compare to a single control. In vivo orthotopic cancer model experiments were analyzed by two-sided one-way ANOVA with Tukey's post hoc analysis to compare all groups. Reported *P* values were assigned $^{***}P < 0.001$, $^{**}P < 0.01$, and $^{*}P < 0.05$, and exact *P* values are reported in captions.

Background subtraction of in vitro solution-based data was conducted using a well in the same plate with identical buffer conditions to the samples. Data were processed with custom MATLAB code, which applied spectral corrections as noted above for wavelength-dependent features in emission intensity, background subtraction, and data fitting of nanotube emission peaks with Lorentzian functions.

Background subtraction for surface-based hyperspectral microscopy was performed by acquiring hyperspectral cubes from an identical glass surface with identical buffer conditions to the samples. Data were processed with custom MATLAB code, which applied spectral corrections for nonuniformity in the camera's light gathering efficiency, background subtraction, and data fitting of emission peaks of individual nanotube species to Lorentzian functions. Binned center wavelengths of all analyzed single nanotubes ($n = 82$ to 100 as noted in Results) were graphed as histograms and fit with Lorentzian functions to obtain total population center wavelengths.

In vivo spectral data were baseline-subtracted with a spline-interpolation method via OriginPro 9 software (OriginLab) instead of blank spectra due to nonuniformity in background spectra dependent on location on the mouse and the distance from the probe (fig. S4). Data were processed with custom MATLAB code, which applied spectral corrections for nonlinearity of the InGaAs detector response and data fitting to Lorentzian functions to obtain emission center wavelengths.

In solution-based experiments, r^2 fit values were not less than 0.98. In surface-based experiments, r^2 fit values were used only if greater than 0.6.

SUPPLEMENTARY MATERIALS

Supplementary material for this article is available at http://advances.sciencemag.org/cgi/content/full/4/4/eaaq1090/DC1

Supplementary Text

fig. S1. Characterization of sensor function in vitro.

fig. S2. Single-sensor HE4 response characterization.

fig. S3. Images taken during the procedure to surgically implant the sensor devices.

fig. S4. Baseline subtraction procedure of a spectrum obtained from the implanted sensor device in vivo (E^3 = one thousand units).

fig. S5. Raw and fitted sensor data from all mice in the exogenous protein injection experiment.

fig. S6. H&E stain of tumor nodules in tissue resected from each murine model of ovarian cancer.

fig. S7. Sensor implant emission data from all murine orthotopic ovarian cancer models.

fig. S8. In vivo sensor stability.

table S1. Change in the nanotube emission wavelength of the DNA-SWCNT following conjugation of the anti-HE4 antibody to the DNA.

table S2. Concentration of HE4 in conditioned cell culture media and ascites from representative mouse ascites samples as determined by ELISA of SK-OV-3, OVCAR-8, OVCAR-3, and OVCAR-5 models in vitro and in vivo.

REFERENCES AND NOTES

1. International Agency for Research on Cancer, *Global Cancer Statistics*; http://globocan.iarc.fr/Pages/fact_sheets_population.aspx [accessed 2 July 2016].
2. G. C. Jayson, E. C. Kohn, H. C. Kitchener, J. A. Ledermann, Ovarian cancer. *Lancet* **384**, 1376–1388 (2014).
3. R. L. Siegel, K. D. Miller, A. Jemal, Cancer statistics, 2016. *CA Cancer J. Clin.* **66**, 7 (2016).
4. National Cancer Institute, Surveillance, Epidemiology, and End Results Program; https://seer.cancer.gov/statfacts/html/all.html [accessed 2 July 2016].

5. S. Vaughan, J. I. Coward, R. C. Bast Jr., A. Berchuck, J. S. Berek, J. D. Brenton, G. Coukos, C. C. Crum, R. Drapkin, D. Etemadmoghadam, M. Friedlander, H. Gabra, S. B. Kaye, C. J. Lord, E. Lengyel, D. A. Levine, I. A. McNeish, U. Menon, G. B. Mills, K. P. Nephew, A. M. Oza, A. K. Sood, E. A. Stronach, H. Walczak, D. D. Bowtell, F. R. Balkwill, Rethinking ovarian cancer: Recommendations for improving outcomes. *Nat. Rev. Cancer* **11**, 719–725 (2011).
6. C. Maringe, S. Walters, J. Butler, M. P. Coleman, N. Hacker, L. Hanna, B. J. Mosgaard, A. Nordin, B. Rosen, G. Engholm, M. L. Gjerstorff, J. Hatcher, T. B. Johannesen, C. E. McGahan, D. Meechan, R. Middleton, E. Tracey, D. Turner, M. A. Richards, B. Rachet ICBP Module 1 Working Group, Stage at diagnosis and ovarian cancer survival: Evidence from the International Cancer Benchmarking Partnership. *Gynecol. Oncol.* **127**, 75–82 (2012).
7. V. A. Moyer; U.S. Preventive Services Task Force, Screening for ovarian cancer: U.S. Preventive Services Task Force reaffirmation recommendation statement. *Ann. Intern. Med.* **157**, 900–904 (2012).
8. S. S. Buys, E. Partridge, A. Black, C. C. Johnson, L. Lamerato, C. Isaacs, D. J. Reding, R. T. Greenlee, L. A. Yokochi, B. Kessel, E. David Crawford, T. R. Church, G. L. Andriole, J. L. Weissfeld, M. N. Fouad, D. Chia, B. O'Brien, L. R. Ragard, J. D. Clapp, J. M. Rathmell, T. L. Riley, P. Hartge, P. F. Pinsky, C. S. Zhu, G. Izmirlian, B. S. Kramer, A. B. Miller, J.-L. Xu, P. C. Prorok, J. K. Gohagan, C. D. Berg; PLCO Project Team, Effect of screening on ovarian cancer mortality. *JAMA* **305**, 2295–2303 (2011).
9. B. Zhang, F. F. Cai, X. Y. Zhong, An overview of biomarkers for the ovarian cancer diagnosis. *Eur. J. Obstet. Gynecol. Reprod. Biol.* **158**, 119–123 (2011).
10. R. G. Moore, E. K. Hill, T. Horan, N. Yano, K. K. Kim, S. MacLaughlan, G. Lambert-Messerlian, Y. T. D. Tseng, J. F. Padbury, M. C. Miller, T. S. Lange, R. K. Singh, HE4 (WFDC2) gene overexpression promotes ovarian tumor growth. *Sci. Rep.* **4**, 3574 (2014).
11. R. Drapkin, H. H. von Horsten, Y. Lin, S. C. Mok, C. P. Crum, W. R. Welch, J. L. Hecht, Human epididymis protein 4 (HE4) is a secreted glycoprotein that is overexpressed by serous and endometrioid ovarian carcinomas. *Cancer Res.* **65**, 2162–2169 (2005).
12. I. Hellström, J. Raycraft, M. Hayden-Ledbetter, J. A. Ledbetter, M. Schummer, M. McIntosh, C. Drescher, N. Urban, K. E. Hellström, The HE4 (WFDC2) protein is a biomarker for ovarian carcinoma. *Cancer Res.* **63**, 3695–3700 (2003).
13. M. A. Karlsen, N. Sandhu, C. Høgdall, I. J. Christensen, L. Nedergaard, L. Lundvall, S. A. Engelholm, A. T. Pedersen, D. Hartwell, M. Lydolph, I. A. Laursen, E. V. S. Høgdall, Evaluation of HE4, CA125, risk of ovarian malignancy algorithm (ROMA) and risk of malignancy index (RMI) as diagnostic tools of epithelial ovarian cancer in patients with a pelvic mass. *Gynecol. Oncol.* **127**, 379–383 (2012).
14. V. O. Shender, M. S. Pavlyukov, R. H. Ziganshin, G. P. Arapidi, S. I. Kovalchuk, N. A. Anikanov, I. A. Altukhov, D. G. Alexeev, I. O. Butenko, A. L. Shavarda, E. B. Khomyakova, E. Evtushenko, L. A. Ashrafyan, I. B. Antonova, I. N. Kuznetcov, A. Y. Gorbachev, M. I. Shakhparonov, V. M. Govorun, Proteome–metabolome profiling of ovarian cancer ascites reveals novel components involved in intercellular communication. *Mol. Cell. Proteomics* **13**, 3558–3571 (2014).
15. D. A. Levine, U.S. Patent 20,130,078,319 (2013).
16. C. S. Clair, J. Ducie, Q. Zhou, F. Dao, N. Kauff, D. Spriggs, M. Fleisher, A. Iasonos, D. Levine, Uterine washing biomarkers as a novel screening tool for high-grade serous carcinoma. *Gynecol. Oncol.* **130**, e71 (2013).
17. D. Ghosh, A. F. Bagley, Y. J. Na, M. J. Birrer, S. N. Bhatiaand, A. M. Belcher, Deep, noninvasive imaging and surgical guidance of submillimeter tumors using targeted M13-stabilized single-walled carbon nanotubes. *Proc. Natl. Acad. Sci. U.S.A.* **111**, 13948–13953 (2014).
18. I. E. Araci, B. Su, S. R. Quake, Y. Mandel, An implantable microfluidic device for self-monitoring of intraocular pressure. *Nat. Med.* **20**, 1074–1078 (2014).
19. J. M. Dubach, D. I. Harjes, H. A. Clark, Ion-selective nano-optodes incorporating quantum dots. *J. Am. Chem. Soc.* **129**, 8418–8419 (2007).
20. X. Zheng, H. Mao, D. Huo, W. Wu, B. Liu, X. Jiang, Successively activatable ultrasensitive probe for imaging tumour acidity and hypoxia. *Nat. Biomed. Eng.* **1**, 0057 (2017).
21. M. J. O'Connell, S. M. Bachilo, C. B. Huffman, V. C. Moore, M. S. Strano, E. H. Haroz, K. L. Rialon, P. J. Boul, W. H. Noon, C. Kittrell, J. Ma, R. H. Hauge, R. Bruce Weisman, R. E. Smalley, Band gap fluorescence from individual single-walled carbon nanotubes. *Science* **297**, 593–596 (2002).
22. K. Welsher, S. P. Sherlock, H. Dai, Deep-tissue anatomical imaging of mice using carbon nanotube fluorophores in the second near-infrared window. *Proc. Natl. Acad. Sci. U.S.A.* **108**, 8943–8948 (2011).
23. D. A. Heller, S. Baik, T. E. Eurell, M. S. Strano, Single-walled carbon nanotube spectroscopy in live cells: towards long-term labels and optical sensors. *Adv. Mater.* **17**, 2793–2799 (2005).
24. D. A. Heller, H. Jin, B. M. Martinez, D. Patel, B. M. Miller, T. K. Yeung, P. V. Jena, C. Höbartner, T. Ha, S. K. Silverman, M. S. Strano, Multimodal optical sensing and analyte specificity using single-walled carbon nanotubes. *Nat. Nanotechnol.* **4**, 114–120 (2008).
25. J. Zhang, M. P. Landry, P. W. Barone, J. H. Kim, S. Lin, Z. W. Ulissi, D. Lin, B. Mu, A. A. Boghossian, A. J. Hilmer, A. Rwei, A. C. Hinckley, S. Kruss, M. A. Shandell, N. Nair, S. Blake, F. Şen, S. Şen, R. G. Croy, D. Li, K. Yum, J. H. Ahn, H. Jin, D. A. Heller, J. M. Essigmann, D. Blankschtein, M. S. Strano, Molecular recognition using corona phase complexes made of synthetic polymers adsorbed on carbon nanotubes. *Nat. Nanotechnol.* **8**, 959–968 (2013).
26. D. Roxbury, P. V. Jena, Y. Shamay, C. P. Horoszko, D. A. Heller, Cell membrane proteins modulate the carbon nanotube optical bandgap via surface charge accumulation. *ACS Nano* **10**, 499–506 (2016).
27. N. M. Iverson, P. W. Barone, M. Shandell, L. J. Trudel, S. Sen, F. Sen, V. Ivanov, E. Atolia, E. Farias, T. P. McNicholas, N. Reuel, N. M. A. Parry, G. N. Wogan, M. S. Strano, In vivo biosensing via tissue-localizable near-infrared-fluorescent single-walled carbon nanotubes. *Nat. Nanotechnol.* **8**, 873–880 (2013).
28. J. D. Harvey, P. V. Jena, H. A. Baker, G. H. Zerze, R. M. Williams, T. V. Galassi, D. Roxbury, J. Mittal, D. A. Heller, A carbon nanotube reporter of microRNA hybridization events in vivo. *Nat. Biomed. Eng.* **1**, 0041 (2017).
29. S. Barua, J.-W. Yoo, P. Kolhar, A. Wakankar, Y. R. Gokarn, S. Mitragotri, Particle shape enhances specificity of antibody-displaying nanoparticles. *Proc. Natl. Acad. Sci. U.S.A.* **110**, 3270–3275 (2013).
30. B. A. Larsen, P. Deria, J. M. Holt, I. N. Stanton, M. J. Heben, M. J. Therien, J. L. Blackburn, Effect of solvent polarity and electrophilicity on quantum yields and solvatochromic shifts of single-walled carbon nanotube photoluminescence. *J. Am. Chem. Soc.* **134**, 12485–12491 (2012).
31. B. Sweryda-Krawiec, H. Devaraj, G. Jacob, J. J. Hickman, A new interpretation of serum albumin surface passivation. *Langmuir* **20**, 2054–2056 (2004).
32. J. Budhathoki-Uprety, P. V. Jena, D. Roxbury, D. A. Heller, Helical polycarbodiimide cloaking of carbon nanotubes enables inter-nanotube exciton energy transfer modulation. *J. Am. Chem. Soc.* **136**, 15545–15550 (2014).
33. K. Huhtinen, P. Suvitie, J. Hiissa, J. Junnila, J. Huvila, H. Kujari, M. Setälä, P. Härkki, J. Jalkanen, J. Fraser, J. Mäkinen, A. Auranen, M. Poutanen, A. Perheentupa, Serum HE4 concentration differentiates malignant ovarian tumours from ovarian endometriotic cysts. *Br. J. Cancer* **100**, 1315–1319 (2009).
34. D. Roxbury, P. V. Jena, R. M. Williams, B. Enyedi, P. Niethammer, S. Marcet, M. Verhaegen, S. Blais-Ouellette, D. A. Heller, Hyperspectral microscopy of near-infrared fluorescence enables 17-chirality carbon nanotube imaging. *Sci. Rep.* **5**, 14167 (2015).
35. T. V. Galassi, P. V. Jena, D. Roxbury, D. A. Heller, Single nanotube spectral imaging to determine molar concentrations of isolated carbon nanotube species. *Anal. Chem.* **89**, 1073–1077 (2017).
36. P. V. Jena, D. Roxbury, T. V. Galassi, L. Akkari, C. P. Horoszko, D. B. Iaea, J. Budhathoki-Uprety, N. Pipalia, A. S. Haka, J. D. Harvey, J. Mittal, F. R. Maxfield, J. A. Joyce, D. A. Heller, A carbon nanotube optical reporter maps endolysosomal lipid flux. *ACS Nano* **11**, 10689–10703 (2017).
37. H. Zheng, Y. Gao, Serum HE4 as a useful biomarker in discriminating ovarian cancer from benign pelvic disease. *Int. J. Gynecol. Cancer* **22**, 1000–1005 (2012).
38. A. Chudecka-Głaz, A. Cymbaluk-Płoska, J. Menkiszak, A. Sompolska-Rzechuła, E. Byra, I. Rzepka-Górska, HE4 tumor marker concentration in neoplastic peritoneal effusion and in peritoneal fluid associated with benign gynecological diseases. *J. Ovarian Res.* **7**, 22 (2014).
39. M. Zheng, A. Jagota, E. D. Semke, B. A. Diner, R. S. Mclean, S. R. Lustig, R. E. Richardson, N. G. Tassi, DNA-assisted dispersion and separation of carbon nanotubes. *Nat. Mater.* **2**, 338–342 (2003).
40. S. Domcke, R. Sinha, D. A. Levine, C. Sander, N. Schultz, Evaluating cell lines as tumour models by comparison of genomic profiles. *Nat. Commun.* **4**, 2126 (2013).
41. X. Michalet, F. F. Pinaud, L. A. Bentolila, J. M. Tsay, S. Doose, J. J. Li, G. Sundaresan, A. M. Wu, S. S. Gambhir, S. Weiss, Quantum dots for live cells, in vivo imaging, and diagnostics. *Science* **307**, 538–544 (2005).
42. X. Yu, B. Munge, V. Patel, G. Jensen, A. Bhirde, J. D. Gong, S. N. Kim, J. Gillespie, J. S. Gutkind, F. Papadimitrakopoulos, J. F. Rusling, Carbon nanotube amplification strategies for highly sensitive immunodetection of cancer biomarkers. *J. Am. Chem. Soc.* **128**, 11199–11205 (2006).
43. J. Zhang, S. Kruss, A. J. Hilmer, S. Shimizu, Z. Schmois, F. De La Cruz, P. W. Barone, N. F. Reuel, D. A. Heller, M. S. Strano, A rapid, direct, quantitative, and label-free detector of cardiac biomarker troponin T using near-infrared fluorescent single-walled carbon nanotube sensors. *Adv. Healthc. Mater.* **3**, 412–423 (2014).
44. X. Tu, S. Manohar, A. Jagota, M. Zheng, DNA sequence motifs for structure-specific recognition and separation of carbon nanotubes. *Nature* **460**, 250–253 (2009).
45. C. R. Behrens, B. Liu, in *Mabs* (Landes Bioscience, 2013), vol. 6, pp. 46–53.
46. R. M. Williams, L. J. Sooter, In vitro selection of cancer cell-specific molecular recognition elements from amino acid libraries. *J. Immunol. Res.* **2015**, 186586 (2015).
47. R. M. Williams, C. J. Hajiran, S. Nayeem, L. J. Sooter, Identification of an antibody fragment specific for androgen-dependent prostate cancer cells. *BMC Biotechnol.* **14**, 81 (2014).
48. R. Yang, Z. Tang, J. Yan, H. Kang, Y. Kim, Z. Zhu, W. Tan, Noncovalent assembly of carbon nanotubes and single-stranded DNA: an effective sensing platform for probing biomolecular interactions. *Anal. Chem.* **80**, 7408–7413 (2008).

49. R. M. Williams, S. Nayeem, B. D. Dolash, L. J. Sooter, The effect of DNA-dispersed single-walled carbon nanotubes on the polymerase chain reaction. *PLOS ONE* **9**, e94117 (2014).
50. J. J. Casciari, M. G. Hollingshead, M. C. Alley, J. G. Mayo, L. Malspeis, S. Miyauchi, M. R. Grever, J. N. Weinstein, Growth and chemotherapeutic response of cells in a hollow-fiber in vitro solid tumor model. *J. Natl. Cancer Inst.* **86**, 1846–1852 (1994).
51. M. Suggitt, D. J. Swaine, G. R. Pettit, M. C. Bibby, Characterization of the hollow fiber assay for the determination of microtubule disruption in vivo. *Clin. Cancer Res.* **10**, 6677–6685 (2004).
52. N. Wisniewski, M. Reichert, Methods for reducing biosensor membrane biofouling. *Colloids Surf. B Biointerfaces* **18**, 197–219 (2000).
53. S. Alidori, D. L. J. Thorek, B. J. Beattie, D. Ulmert, B. Aristega Almeida, S. Monette, D. A. Scheinberg, M. R. McDevitt, Carbon nanotubes exhibit fibrillar pharmacology in primates. *PLOS ONE* **12**, e0183902 (2017).
54. N. Goldstuck, T. Hasskamp, S. Jandi, A. Pett, D. Wildemeersch, Geometric foundations of intrauterine device complications and implications for IUD users–importance of the iud size to maximize tolerability and prevent early discontinuation. *J. Reprod. Med. Endocrinol.* **12**, 255–259 (2016).
55. T. S. Frank, S. A. Manley, O. I. Olopade, S. Cummings, J. E. Garber, B. Bernhardt, K. Antman, D. Russo, M. E. Wood, L. Mullineau, C. Isaacs, B. Peshkin, S. Buys, V. Venne, P. T. Rowley, S. Loader, K. Offit, M. Robson, H. Hampel, D. Brener, E. P. Winer, S. Clark, B. Weber, L. C. Strong, A. Thomas, Sequence analysis of BRCA1 and BRCA2: Correlation of mutations with family history and ovarian cancer risk. *J. Clin. Oncol.* **16**, 2417–2425 (1998).
56. T. Riman, I. Persson, S. Nilsson, Hormonal aspects of epithelial ovarian cancer: Review of epidemiological evidence. *Clin. Endocrinol.* **49**, 695–707 (1998).
57. R. Bell, M. Petticrew, T. Sheldon, The performance of screening tests for ovarian cancer: Results of a systematic review. *BJOG* **105**, 1136–1147 (1998).
58. D. K. Armstrong, Relapsed ovarian cancer: Challenges and management strategies for a chronic disease. *Oncologist* **7**, 20–28 (2002).
59. T. Van Gorp, I. Cadron, E. Despierre, A. Daemen, K. Leunen, F. Amant, D. Timmerman, B. De Moor, I. Vergote, HE4 and CA125 as a diagnostic test in ovarian cancer: prospective validation of the risk of ovarian malignancy algorithm. *Br. J. Cancer* **104**, 863–870 (2011).
60. G. Zheng, F. Patolsky, Y. Cui, W. U. Wang, C. M. Lieber, Multiplexed electrical detection of cancer markers with nanowire sensor arrays. *Nat. Biotechnol.* **23**, 1294–1301 (2005).

Acknowledgments: We would like to thank D. Spriggs for cell lines; P. Jena and D. Roxbury for instrument automation and MATLAB code and helpful discussions; J. Budhathoki-Uprety, Y. Shamay, R. Frederiksen, J. Kubala, L. Forbes, D. Deep, and S. Albanese for assistance with the preliminary sensor development and helpful discussions; and R. Drapkin for helpful discussions. We would also like to acknowledge the Molecular Cytology Core Facility and the Small Animal Imaging Core Facility at MSKCC. **Funding:** This work was supported by the NIH New Innovator Award (DP2-HD075698), the NIH Cancer Center Support Grant (P30 CA008748), the Honorable Tina Brozman Foundation for Ovarian Cancer Research, the Louis V. Gerstner Jr. Young Investigator's Fund, the Frank A. Howard Scholars Program, the Alan and Sandra Gerry Metastasis Research Initiative, the Center for Molecular Imaging and Nanotechnology at MSKCC, Cycle for Survival, the Anna Fuller Fund, Mr. William H. Goodwin and Mrs. Alice Goodwin and the Commonwealth Foundation for Cancer Research, the Imaging and Radiation Sciences Program, and the Experimental Therapeutics Center at MSKCC. R.M.W. was supported by the Ovarian Cancer Research Fund (Ann Schreiber Mentored Investigator Award 370463) and the American Heart Association Postdoctoral Fellowship (17POST33650043). T.V.G. was supported by the Frank Lappin Horsfall Jr. Fellowship. M.S. was supported by the Hunter R. Rawlings III Cornell Presidential Research Scholars program and the Gerstner Sloan Kettering Summer Undergraduate Research Program. D.A.L. is supported in part by grants from the U.S. Department of Defense (W81XWH-11-2-0230 and W81XWH-15-1-0429). **Author contributions:** R.M.W., D.A.L., and D.A.H. conceived and wrote the manuscript. R.M.W., C.L., T.V.G., J.D.H., R.L., M.S., M.A.D., and J.S. performed the experiments and data analysis. N.O., F.D., and D.A.L. obtained and processed the patient samples. All authors provided input and feedback for manuscript preparation. **Competing interests:** D.A.L. is an inventor on a patent application related to this work (application no. PCT/US2012/056776, filed on 22 September 2012). D.A.H. and R.M.W. are inventors on another patent application related to this work applied for by MSKCC (application no. PCT/US2017/026563, filed on 7 April 2017). The other authors declare that they have no competing interests. **Data and materials availability:** All data needed to evaluate the conclusions in the paper are present in the paper and/or the Supplementary Materials. Additional data related to this paper may be requested from the authors.

Submitted 2 October 2017
Accepted 6 March 2018
Published 18 April 2018
10.1126/sciadv.aaq1090

Citation: R. M. Williams, C. Lee, T. V. Galassi, J. D. Harvey, R. Leicher, M. Sirenko, M. A. Dorso, J. Shah, N. Olvera, F. Dao, D. A. Levine, D. A. Heller, Noninvasive ovarian cancer biomarker detection via an optical nanosensor implant. *Sci. Adv.* **4**, eaaq1090 (2018).